ISMAR: an airborne submillimetre radiometer

Stuart Fox[1], Clare Lee[1], Brian Moyna[2], Martin Philipp[3], Ian Rule[1], Stuart Rogers[1], Robert King[1], Matthew Oldfield[2], Simon Rea[2], Manju Henry[2], Hui Wang[2], and R. Chawn Harlow[1]

[1]Met Office, FitzRoy Road, Exeter, UK, EX1 3PB
[2]Rutherford Appleton Laboratory, Harwell Campus, Didcot, UK, OX11 0QX
[3]RPG Radiometer Physics GmbH, Werner-von-Siemens-Str. 4, 53340 Meckenheim, Germany

Correspondence to: S. Fox
(stuart.fox@metoffice.gov.uk)

Abstract. The International Submillimetre Airborne Radiometer (ISMAR) has been developed as an airborne demonstrator for the Ice Cloud Imager (ICI) that will be launched on board the next generation of European polar-orbiting weather satellites in the 2020s. It currently has 15 channels at frequencies between 118GHz and 664GHz which are sensitive to scattering by cloud ice, and additional channels at 874GHz are being developed. This paper presents an overview of ISMAR and describes the algorithms used for calibration. The main sources of bias in the measurements are evaluated, as well as the radiometric sensitivity in different measurement scenarios. It is shown that for downwards views from high altitude, representative of a satellite viewing geometry, the bias in most channels is less than ±1K and the NEΔT is less than 2K, with many channels having an NEΔT less than 1K. In-flight calibration accuracy is also evaluated by comparison of high-altitude zenith views with radiative transfer simulations.

1 Introduction

ISMAR (International Submillimetre Airborne Radiometer) is a new airborne passive remote sensing instrument which has been jointly funded by the Met Office and the European Space Agency (ESA). It first flew in 2014 and contains a number of heterodyne receivers operating at frequencies between 118 and 664GHz. The instrument has a modular design allowing additional channels to be added, and receivers at 874GHz are being developed. The current receiver front-ends were designed and built by Rutherford Appleton Laboratory (RAL) Space and Radiometer Physics GmbH (RPG), and the IF back ends were built by Thales Alenia Space. The rest of the instrument design, build and aircraft installation were carried out by RAL, the Met Office, Cranfield Aerospace and BAE Systems.

Previous theoretical studies (e.g. Evans and Stephens, 1995; Evans et al., 1998; Buehler et al., 2007; Jiménez et al., 2007) have suggested that passive submillimetre radiometers can be used for satellite retrievals of ice cloud properties including ice water path, particle size and cloud altitude, which have an important impact on weather and climate prediction (see, for example Waliser et al., 2009). Submillimetre observations have also been suggested for precipitation retrieval e.g. the GEM (Staelin et al., 1998) and GOMAS (Bizzari et al., 2005) satellite proposals, and characterisation of volcanic ash plumes (Baran, 2012). The Ice Cloud Imager (ICI) is a submillimetre radiometer due to be launched on board the MetOp second generation

satellite in the 2020s (Kangas et al., 2012). ISMAR has been developed as an airborne demonstrator for ICI, and can be used for developing retrieval algorithms prior to the launch of ICI, as well as for scientific case studies and calibration/validation post-launch.

ISMAR has been certified to fly on the FAAM BAe-146 Atmospheric Research Aircraft, which carries complementary
5   instruments measuring basic atmospheric parameters, microwave radiometers, infra-red and visible spectrometers, a downward pointing backscatter lidar and in-situ cloud physics probes. Dropsondes can be used to obtain profiles of temperature, humidity and wind below the aircraft.

This paper gives an overview of the design and performance of ISMAR, and is arranged as follows: Sect. 2 describes the instrument design and Sect. 3 describes the methods used to process the data. Section 4 considers the sources of systematic
10 error (bias) in the ISMAR measurements and Sect. 5 discusses the radiometric sensitivity. In-flight performance is evaluated in Sect. 6 by comparing high-altitude zenith views with radiative transfer simulations, and conclusions are given in Sect. 7

2   Instrument design

ISMAR has a self-contained design, with the receivers, calibration targets, scan mechanism and control electronics contained in a single package with dimensions of approximately $1.1 \times 0.4 \times 0.5 \mathrm{m}$ and a weight of around 90kg. An ethernet port allows
15 an operator to monitor and control the instrument during flight. The instrument is installed in the radiometer blister on the front port side of the FAAM BAe-146 allowing unobstructed upward and downward views (Fig. 1), and in future it could also be flown on other high-altitude aircraft.

ISMAR currently has 7 heterodyne receivers providing 15 channels. These are centred on the oxygen absorption line at 118.75GHz (5 channels), the water-vapour absorption lines at 325.15 and 448GHz (3 channels each), and atmospheric quasi-
20 windows at 243.2, and 664GHz. All the channels have dual side-bands. The window channels each have two receivers to measure dual polarisations which gives information about ice particle shape and alignment (Evans et al., 1998). ISMAR has a modular design that allows additional channels to be added as they become available. Further quasi-window receivers at 874.4GHz are currently being developed which will give greater sensitivity to small ice particles, and a receiver centred on the 424.7GHz oxygen absorption line is also planned. A full overview of the ISMAR channels, including measurements of system
25 noise temperature, is given in Table 1, and the RF design schematic is shown in Fig. 2. In addition to ISMAR, receivers centred at 23.8, 50.1, 89, 157 and 183GHz are provided by the Deimos (Hewison, 1995) and MARSS (McGrath and Hewison, 2001) microwave radiometers on board the aircraft. Together these instruments give a close match to the ICI channels, and contain a significant subset of the proposed GOMAS channels.

A schematic of ISMAR is shown in Fig. 3. The front-end contains an array of feedhorns and associated local oscillators,
30 frequency multipliers and mixers and the back-end carries the intermediate-frequency (IF) filters, amplifiers and detectors. PTFE lenses, blazed to reduce reflections at each frequency, are used to reduce the half-power beam width (HPBW) for all channels to less than $4°$. The array of feedhorns directly views a rotating gold-coated planar scan mirror angled at $45°$ which directs their field of view on to one of two internal blackbody calibration targets or the external scenes. The gold coating has

a thickness of 5μm, which is significantly larger than the penetration depth of the radiation at all the ISMAR frequencies. The scan mirror is heated to prevent frosting or condensation during flight. The direct-view design eliminates losses due to traditional quasi-optical components but requires a larger scan mirror and calibration targets. To save space the front-end is housed inside the frameless scan motor. The scan direction is along-track, with nadir views between a nominal +50° and -10°

5 and zenith views between +10° and -40°, where positive scan angles are associated with views in the forward direction as illustrated in Fig. 3. The true scan angles can vary from the nominal angles by a few degrees due to the mounting angle of the instrument on the aircraft and changes in aircraft pitch during flight. The scan pattern is fully configurable through software. A typical scan pattern taking approximately 4s will start at the forward (heated) calibration target and step through 7 nadir views, the aft (unheated) calibration target, and 6 zenith views.

10 The design of the scanning mechanism means that the polarisation detected by each receiver varies with scan angle and aircraft attitude. The polarisations are selected such that the single-polarisation channels detect vertical polarisation and the dual-polarisation channels detect horizontal and vertical polarisation when the instrument is viewing the +50° nadir direction during straight and level flight. This gives the closest match to the conical scanning geometry of ICI.

The gain of the ISMAR receivers is temperature dependent so active thermal control is used to maintain a constant temper-

15 ature. Frequent in-flight views of the two black-body calibration targets (designed and built by RAL) are also used to provide continuous calibration. One of the targets is actively heated to 353K using a printed circuit heater element laminated to the back of the target substrate, whilst the other is allowed to drift, typically being slightly warmer than the ambient temperature due to the thermal conditions inside the radiometer blister. In order to reduce the rate of heat loss from the heated target it is protected from airflow by a 8μm polypropylene window stretched over the front of the target. Laboratory testing has shown that

20 there are no adverse radiometric effects attributable to the window. The calibration targets are based on prototype designs developed for the ALMA telescope and consist of pyramidal structures with base 10mm and height 40mm coated with Eccosorb CR-114 absorber. The substrate is machined from magnesium alloy to save weight. The measurements of Murk et al. (2008) indicate that the monostatic return loss from the calibration targets should be greater than 50dB at ISMAR frequencies. Target temperatures are monitored by up to ten Minco type S9688PA1X12 platinum resistance thermometers (PRTs) embedded in the

25 target substrates. These PRTs are at a depth of 30mm from the rear face of the target and 20mm from the tips of the pyramids. Additional PRTs located at depths of 15mm and 50mm from the rear face of the target can be used to monitor thermal gradients within the substrate (see Fig. 4). The target PRTs have been individually calibrated against a traceable standard.

The voltage output from each detector passes through a two-stage video amplifier where a precision voltage offset is applied to ensure the signal remains within the range of the A/D converter. The video amplifier also acts as a low-pass filter with a

30 cut-off frequency of 1kHz. The output from the video amplifier is digitally sampled and averaged using a National Instruments CompactRIO embedded controller. The sampling rate and overall integration time is software configurable with a typical integration period of 100ms. The controller is also used to drive the scan mechanism and to monitor and control the IF amplifier, scan mirror and calibration target temperatures.

Atmospheric
Measurement
Techniques
Discussions

3 Calibration and processing

This section describes the calibration procedure used to derive scene brightness temperatures from the receiver voltages. Each ISMAR channel is assumed to output a voltage V_{scene} that varies linearly with received power from the scene, P_{scene} according to

$$P_{\mathrm{scene}} = \frac{V_{\mathrm{scene}}}{G} - P_{\mathrm{rec}}. \tag{1}$$

The linear gain, G and offset P_{rec} are calculated using the calibration target views by

$$G = \frac{\overline{V_{\mathrm{hot}}} - \overline{V_{\mathrm{cold}}}}{\overline{P_{\mathrm{hot}}} - \overline{P_{\mathrm{cold}}}} \tag{2}$$

$$P_{\mathrm{rec}} = \frac{\overline{V_{\mathrm{cold}}}}{G} - \overline{P_{\mathrm{cold}}}. \tag{3}$$

The overbar represents the mean value for all calibration views within a 60 second window centred on the time of the scene view. This time window has been selected to minimise the noise in the measured brightness temperatures (see Sect. 5). The received powers from the hot and cold calibration targets are calculated from the target temperatures as described below. Deviations in the receiver output from the linear response Eq. (1) will give errors in calibrated brightness temperature and a correction is required for some ISMAR channels as described in Sect. 4.4.

It is common when calibrating microwave radiometers to assume that the received power from a black body is linearly related to its temperature, allowing temperatures to be used in place of received power in the above equations (see the discussion in Han and Westwater, 2000, for example). Equation (1) then gives a direct measurement of the scene brightness temperature. However, at the largest frequencies used by ISMAR the linear assumption is no longer valid and a more accurate approximation is required as described below.

The power received by a radiometer when viewing a black-body at temperature T is given by

$$P = \int \frac{h\nu}{\exp^{h\nu/kT} - 1} W(\nu)\mathrm{d}\nu, \tag{4}$$

where h is Plank's constant, k is Boltzmann's constant, ν is frequency and $W(\nu)$ is the channel passband shape which, for a dual sideband receiver, includes both of the sidebands and any sideband imbalance. Equation (4) can be obtained by integrating Eq. 1.17 from Jones (1995), weighted according to the channel passband shape. For ISMAR calibration a suitably accurate approximation to (4) can be made by assuming that the integrand in (4) varies linearly across each of the channel sidebands and there is no sideband imbalance (sideband imbalance is less than $\pm 1\mathrm{dB}$ for all ISMAR channels). This gives

$$P \approx \left(\frac{h\nu_{\mathrm{low}}}{\exp^{h\nu_{\mathrm{low}}/kT} - 1} + \frac{h\nu_{\mathrm{hi}}}{\exp^{h\nu_{\mathrm{hi}}/kT} - 1} \right) \Delta\nu, \tag{5}$$

where ν_{low} and ν_{hi} are the centre frequencies of the two channel sidebands and $\Delta\nu$ is the channel IF filter bandwidth. For ISMAR calibration Equation (5) is used to calculate the received powers from the hot and cold calibration targets that are required to estimate the receiver gain and offset.

The ISMAR measurements of received scene power are converted to a channel-average Rayleigh-Jeans equivalent brightness temperature defined by

$$T_{\text{scene,rje}} = \frac{P_{\text{scene}}}{k \int W(\nu)\mathrm{d}\nu},$$

(6)

where the approximation in equation (5) implies that $\int W(\nu)\mathrm{d}\nu = 2\Delta\nu$.

As discussed by McGrath and Hewison (2001), non-unity reflectivity Γ of the scan mirror results in contamination of the observed power for both scene and target views

$$\Delta P = (1 - \Gamma)\left(P_{\text{mirror}} - P\right).$$

(7)

In the case of a constant temperature mirror with a constant reflectivity this contamination will be accounted for during the standard calibration process. However, the mirror temperature may not be constant and the reflectivity varies as the detected polarisation relative to the mirror changes through the scan. A theoretical calculation for a plane mirror angled at $45°$ assuming a bulk conductivity of gold of $4.1 \times 10^7 \Omega^{-1}\mathrm{m}^{-1}$ gives reflectivities for parallel and perpendicular polarisations of 0.9984 and 0.9992 respectively at 118GHz, reducing to 0.9957 and 0.9978 at 874GHz. For a constant temperature mirror at 240K viewing a scene with a brightness temperature of 10K this can lead to a change in power correction with scan angle equivalent to a brightness temperature change of up to 0.48K. Equation (7) is therefore used to correct all calibration target and scene views, with P_{mirror} calculated from Eq. (5) using the measured mirror temperature.

4 Calibration biases

This section considers the main sources of bias in the ISMAR measurements. Here we consider a bias to be an error in scene temperature that varies slowly, typically over timescales of minutes or more, and generally in response to changes in the ambient environment. The main sources of bias are errors in the calibration target temperature estimates (section 4.1) and coherent backscatter of leaked local oscillator power from the calibration target leading to standing waves (Sect. 4.2). Some of the ISMAR receivers also have a slightly non-linear response as discussed in Sect. 4.4. Where possible corrections are applied to reduce measurement biases, and estimates are made of the residual uncertainty.

4.1 Calibration target temperatures

Errors in the radiometric temperature of the internal calibration targets lead directly to errors in the target power, and hence the measured antenna temperatures. The temperature required to calculate the target power for each receiver in Eq. (5) is the area average of the absorber surface temperature weighted according to the antenna response pattern. This must be estimated from the measurements made by the PRTs embedded in the substrate of the target. Errors in calibration target temperature arise from a number of sources including errors in the PRT calibrations, and thermal gradients within the targets, both across the target and between the target substrate where the PRTs are located and the surface of the absorber.

Atmospheric
Measurement
Techniques
Discussions

The error in scene brightness temperature $\delta T_{\mathrm{scene,rje}} = T_{\mathrm{scene,measured}} - T_{\mathrm{scene,true}}$ caused by errors in hot and cold target temperatures δT_{hot} and δT_{cold} is approximated by

$$\delta T_{\mathrm{scene,rje}} \approx K\delta T_{\mathrm{hot}} + (1-K)\delta T_{\mathrm{cold}}, \tag{8}$$

where K is the calibration interpolation/extrapolation factor given by

$$K = \frac{T_{\mathrm{scene,rje}} - T_{\mathrm{cold,rje}}}{T_{\mathrm{hot,rje}} - T_{\mathrm{cold,rje}}}. \tag{9}$$

Note that equation (8) relies on the approximation $\mathrm{d}T_{\mathrm{rje}}/\mathrm{d}T \approx 1$ being valid at the calibration target temperatures. At 874GHz and 200K $\mathrm{d}T_{\mathrm{rje}}/\mathrm{d}T = 0.996$ so the errors introduced by this approximation are small. The impact of calibration target temperature errors on the scene brightness temperature error depends on both the scene brightness temperature and the calibration target temperatures. It is greatest when viewing very cold scenes which lie outside the range of the calibration target temperatures, e.g. for zenith views in window channels, and when the temperature difference between the calibration targets temperatures is small. For a typical mid-latitude winter flight the ambient target temperature varies between 285K at low altitude and 245K at high altitude and the heated target temperature is 353K, leading to values of K ranging from -1 to 0.25 for nadir views and -3 to 0 for zenith views.

The individual target PRTs were calibrated against a traceable standard using the Met Office calibration facility. The resistance of each PRT was measured at temperatures between 223K and 323K and a quadratic regression between temperature and resistance was performed. The maximum difference between the quadratic fit and the measured temperature was 0.03K, with many of the PRTs having a maximum error of 0.01K. The bias due to PRT calibration error will therefore be small and can be neglected.

We now consider how to estimate the target temperature over the receiver footprints from the PRT measurements. An indication of thermal gradients across the calibration target is given by the difference in the temperatures measured by the PRTs in different locations. The left-hand plot in figure 5 shows the temperatures measured by the PRTs in the heated calibration target during a time when the aircraft is level at 32000 feet. The small circles indicate the locations of the PRTs and the colour shows the temperature obtained at each point on the target by interpolating between the measurements. Also shown are the -3dB footprints of the receivers, indicated by the larger circles. The centre of the target is warmer than the edges, with a maximum difference of 1.7K between the PRTs. Larger temperature differences (up to 3K) are observed during times when the aircraft is changing altitude. Initially the hot target temperature used for the calibration was derived by weighting the interpolated PRT temperatures according to the antenna footprints. However, it was found that measurement biases with respect to both an external liquid nitrogen cooled target and simulations of zenith brightness temperatures at high altitude could be reduced by using the temperature of the most central PRT for all receivers. This can be justified by noting that thermal images of the heated target in the laboratory suggest that the central hot-spot is much larger than indicated by the interpolated temperatures shown in Fig. 5, which are influenced by the fact that most of the temperature measurements are made close to the edge of the target. Since the channels all have greatest sensitivity near the centre of the target the most central PRT gives the best estimate of the temperature seen by the receivers. The maximum (hot) bias in the heated calibration target due to gradients across the

target is estimated as half the difference between the central PRT and the antenna-averaged interpolated temperature. Values of the hot calibration target temperature bias representative of high-altitude level flight are summarised in Table 2.

The right-hand plot in figure 5 shows the temperatures measured by the PRTs in the ambient calibration target when the aircraft is level at 32000 feet. The temperature gradients are much smaller than for the heated target, with a maximum difference of 0.37K between the PRTs. Much larger temperature differences (up to 4K) can be observed when the aircraft altitude is changing. Since the target is unheated the temperature gradients are expected to be relatively uniform across the target and the antenna-weighted interpolated PRT temperature is used as the best estimate of the ambient target temperature for the calibration. The maximum bias in the ambient target temperature due to gradients across the target is estimated as $\delta T_{cold} = \pm 0.25(T_{max} - T_{min})$, where T_{max} and T_{min} are the maximum and minimum temperatures measured by the PRTs. Where necessary the temperature bias estimate is reduced to ensure that $T_{est} + \delta T_{cold} < T_{max}$ and $T_{est} - \delta T_{cold} > T_{min}$. Table 2 gives typical cold target temperature biases estimated using this method during high altitude level flight.

Due to the relatively low thermal conductivity of the Eccosorb absorber thermal gradients may exist through the thickness of the absorber. Infrared images of the heated target in laboratory conditions show that the tips of the pyramids are significantly cooler than the bulk of the target, but they occupy a very small area so will have a limited impact on the area-weighted target temperature. Unfortunately the infrared camera is not well calibrated and the infrared emissivity of the target is not known so it is not possible to use the images to determine the difference between the surface and PRT temperatures. An order-of-magnitude estimate based on the heater power required to maintain the target in thermal equilibrium, the surface area of the pyramids and the thermal conductivity of the absorber suggests that temperature differences between the substrate and absorber surface of up to 0.3K are possible. Due to the large uncertainty in this estimate no correction is applied to the calibration for gradients through the absorber on the hot target, and they are included in the estimate of bias in Table 2. For the ambient target the temperature differences between the substrate and the surface will be negligible when the target is thermally stable during level flight, but may be significant during aircraft profiles when the target temperature is changing.

4.2 Coherent backscatter

Although the coherent backscatter from the ISMAR calibration targets is expected to be low (Murk et al., 2008, measured less than -50dB for a similar target) there is still the potential for standing waves between the receiver and the target to affect the calibration if sufficient power is radiated from the receiver. Any standing wave will be sensitive to small changes in instrument geometry such as the distance between the receiver and the target and the angle at which the target is viewed. Measurements of the calibration target brightness temperature during small changes in viewing angle can therefore indicate whether standing waves are an issue.

Measurements of the hot and cold calibration target brightness temperatures for a number of viewing angles close to the nominal target position indicate that standing waves are an issue for several ISMAR receivers. Differences with viewing angle of up to 1K, 1.5K and 2K are observed for the 118±3.0GHz, 664-H and 664-V receivers respectively with negligible differences for the other receivers. At 118±3.0GHz the source of the standing wave is leaked power at 121.6GHz from the local oscillators from the 243GHz receivers, whereas at 664GHz the source appears to be the receiver itself.

Atmospheric
Measurement
Techniques
Discussions

Note that coherent backscatter will always increase the voltage observed when viewing a calibration target at a given temperature, hence it is the equivalent of viewing a target at a higher temperature, i.e. a negative value of δT_{hot} or δT_{cold} in equation (8). No corrections are currently applied to account for coherent backscatter because the error is difficult to quantify and may vary through a flight. The maximum target temperature bias estimate for each receiver due to coherent backscatter is given in Table 2.

4.3 Scene temperature bias

The worst-case scene temperature biases due to the target temperature biases described in the previous sections are given in Table 2 for $K = 0.25$ and $K = -2$ which are representative of nadir and zenith views respectively. For nadir views the scene temperature bias is generally less than ± 1K, the exception being the 664GHz receivers which are affected by coherent backscatter. The potential biases are larger (up to 2.6K for receivers not affected by coherent backscatter) for zenith views as the target temperature errors are amplified by the extrapolation from the target temperatures to the low scene temperatures. In the future it may be possible to reduce measurement biases through better characterisation of the calibration target temperatures, and by changing the design of the calibration targets to reduce coherent backscatter.

4.4 Receiver linearity

Departures of the receiver response from the ideal linear response (Eq. (1)) leads to errors in calibrated brightness temperatures. Laboratory tests suggest that the 118GHz and 243-V receivers have a slightly nonlinear response, most likely caused by nonlinearity in the diode detectors. A correction for receiver nonlinearity has been derived by assuming the detector has a quadratic response

$$V_{\mathrm{det}} = k_{\mathrm{D}} P_{\mathrm{D}} + k_{\mathrm{N}} P_{\mathrm{D}}^2, \tag{10}$$

where V_{det} is the detector output voltage, P_{D} is the detector input power, k_{D} is the linear gain of the detector and k_{N} parameterises the detector nonlinearity. The detector input power is given by

$$P_{\mathrm{D}} = k_{\mathrm{PD}}(T_{\mathrm{scene,rje}} + T_{\mathrm{sys}}), \tag{11}$$

where k_{PD} is the total receiver gain prior to the detector and T_{sys} is the system noise temperature.

Substituting (10) and (11) into the calibration equation (1) leads to a scene brightness temperature error

$$\Delta T_{\mathrm{scene,rje}} = \frac{\epsilon(T_{\mathrm{scene,rje}} - T_{\mathrm{hot,rje}})(T_{\mathrm{scene,rje}} - T_{\mathrm{cold,rje}})}{1 + \epsilon(T_{\mathrm{hot,rje}} + T_{\mathrm{cold,rje}} + 2T_{\mathrm{sys}})}, \tag{12}$$

where ϵ is a parameter describing the detector nonlinearity defined by

$$\epsilon = \frac{k_{\mathrm{N}} k_{\mathrm{PD}}}{k_{\mathrm{D}}}. \tag{13}$$

For measurements of a known scene temperature Eq. (12) can be used to derive ϵ. This has been done using laboratory measurements of a liquid nitrogen cooled calibration target. By assuming that $k_{\mathrm{N}}/k_{\mathrm{D}}$ is constant for a given detector and

Atmospheric
Measurement
Techniques
Discussions

Open Access

changes in k_{PD} are proportional to changes in overall linear gain given by (2), the value of ϵ applicable to any scene view can be calculated. Equation (12) is then used to calculate and correct for the nonlinearity in each scene measurement. For scene temperatures close to the calibration target temperatures the nonlinearity correction is small (typically less than 1K for nadir views). However, for very cold scenes such as high-altitude zenith views the correction can be as large as 10K. Attenuators

5 have therefore been added to the 118 and 243-V receivers prior to the detectors, which reduces the effect of the nonlinearity by reducing k_{PD}, at the expense of reducing the dynamic range of the signal. The attenuators were fitted from flight B939 (February 2016) onwards.

5 Sensitivity

The ability of ISMAR to distinguish brightness temperature changes caused by clouds or changes in atmospheric profiles de-

10 pends on the radiometric sensitivity as described by the noise equivalent ΔT (NEΔT). For a total power radiometer like ISMAR with periodic views of calibration loads the NEΔT depends on a number of factors including the scene temperature, system noise temperature, receiver bandwidth, scene and calibration view integration time, time-correlated receiver gain fluctuations, calibration averaging parameters and calibration load temperatures (Hersman and Poe, 1981). It is useful to provide estimates of NEΔT alongside ISMAR measurements to allow the significance of changes in brightness temperature to be assessed.

15 Hersman and Poe (1981) derive an expression for NEΔT in terms of the scan and calibration parameters and the receiver output voltage power spectral density which gives a worst-case estimate when the scene temperature lies between the calibration load temperatures. Since ISMAR uses an ambient temperature target as the cold calibration load rather than the cold space view typically used by satellite radiometers it is possible for the scene temperature to be significantly colder than either calibration load, which can lead to larger NEΔT due to the extrapolation of the derived calibration coefficients. It is relatively simple to

20 extend the analysis to cover this case, leading to an expression of the form

$$
(\mathrm{NE}\Delta\mathrm{T})^2 \approx \frac{T_{\mathrm{sys}}}{\tau_s \Delta\nu} + K^2 \frac{T_{\mathrm{sys}}}{\tau_c \Delta\nu} \sum_{k=1}^{n_{\mathrm{cal}}} w_{\mathrm{hot},k}^2 + (1-K)^2 \frac{T_{\mathrm{sys}}}{\tau_c \Delta\nu} \sum_{k=1}^{n_{\mathrm{cal}}} w_{\mathrm{cold},k}^2
$$

$$
+ \frac{1}{G^2} \int_0^\infty S_g(f) H(f, K, \tau_s, \tau_c, w_{\mathrm{hot},1..n_{\mathrm{cal}}}, w_{\mathrm{cold},1..n_{\mathrm{cal}}}, t_{\mathrm{hot},1..n_{\mathrm{cal}}}, t_{\mathrm{cold},1..n_{\mathrm{cal}}}, t_{\mathrm{scene}}) \mathrm{d}f, \tag{14}
$$

where f is frequency, τ_s is the scene integration time, τ_c is the calibration view integration time, w_{hot} and w_{cold} are the weightings applied to each of the n_{cal} calibration views, t_{hot}, t_{cold} and t_{scene} are the times of the calibration and scene views,

25 $S_g(f)$ is the non-uniform component of the receiver output voltage power spectral density (which includes contributions from time-correlated gain fluctuations) and H is the calibration processing transfer function which has a similar form to that given by Hersman and Poe but includes additional terms and depends on the calibration extrapolation factor K (defined in Eq. (9)).

For receiver noise with a uniform power spectral density $S_g(f) = 0$ (i.e. no time-correlated output fluctuations) the minimum NEΔT is obtained by using a uniform weighting of a large number of calibration views. However, in the presence of

30 non-uniform receiver noise $S_g(f) \sim f^{-n}$, increasing the time over which the calibration views are averaged increases the contribution from the non-uniform noise component which can outweigh the reduction in the contribution of the uniform

component and give an increase in NEΔT. Laboratory measurements of $S_g(f)$ for the ISMAR receivers show that significant non-uniform noise spectral density affects all channels for frequencies representative of the time taken to complete a single scan cycle. The calibration averaging method must therefore be carefully selected to avoid degrading the sensitivity.

The optimum calibration averaging time and weightings in the presence of time-correlated noise depends on both the form of $S_g(f)$ and the value of K. However, for ISMAR processing a uniform weighting of all calibration views within a 60 second window centred on the time of the scene view has been selected. This is simple to implement, gives a relatively constant NEΔT for all values of K, and does not significantly increase the NEΔT above the value that could be obtained by using optimized weightings for each scene view. Table 3 shows the estimated NEΔT calculated using (14) for a typical ISMAR scan pattern for $K = 0.5$ and $K = -3.6$. For comparison, the standard deviation of the measured brightness temperature of a liquid nitrogen cooled external calibration target over a 60 second period is also shown. There is close agreement with the calculated NEΔT for $K = -3.6$ which is the value applicable to these measurements.

6 Flight performance

ISMAR has flown on 17 flights during three measurement campaigns: STICCS (Sub-millimetre Trials In Clear and Cloudy Skies) based in Prestwick (UK) in November and December 2014, COSMICS (Cold-air Outbreak and Sub-millimetre Ice Cloud Studies) based in Prestwick and Keflavik (Iceland) during March 2015 and WINTEX-16 based in Cranfield (UK) during February and March 2016. The locations and times of the campaigns were chosen to maximise the opportunities to fly above cirrus cloud given the maximum altitude of the FAAM aircraft of 35000 feet (approximately 11km). In this section the in-flight performance of ISMAR is assessed by comparing high-altitude zenith views in clear skies with radiative transfer simulations.

Above the tropopause the atmospheric absorption and emission due to water vapour is very small. Away from oxygen absorption lines the zenith brightness temperatures are dominated by the cold space background so uncertainties in radiative transfer simulations are expected to be small. These cold scene brightness temperatures also represent a challenging measurement as they require significant extrapolation from the calibration target temperatures. The top row of Fig. 6 shows the zenith measurements made during two flights (B893 and B940) where the aircraft was in straight and level flight above the tropopause. Also shown are radiative transfer simulations performed using ARTS (Eriksson et al., 2011). Absorption and emission due to water vapour and oxygen were calculated using the complete absorption models of Rosenkranz (1998, 1993) and ozone lines were taken from the HITRAN database (Rothman et al., 2013). The profiles of temperature and water vapour were taken from short-term Met Office forecast models valid at the time of the measurements, and a monthly climatology was used for the ozone profile. Ozone absorption and emission makes a significant contribution to zenith brightness temperatures at frequencies of 325GHz and above.

The bottom row of Fig. 6 shows the difference between the measured and simulated brightness temperatures. The maximum estimated bias in the measurements due calibration target temperature bias and standing wave effects are also indicated. The majority of the measurements are consistent with the simulations, with small biases even at these very low scene temperatures. The main differences occur for the 118±1.1GHz, 118±1.5GHz and 448±1.4GHz channels which are close to the centre of the

gaseous absorption lines and are most sensitive to errors in the input profiles of temperature and humidity. Larger discrepancies are also seen for the channels where standing wave effects increase the calibration uncertainty.

7   Conclusions

The ISMAR radiometer has been developed as an airborne demonstrator for ICI and has flown on the FAAM BAe-146 during a number of measurement campaigns. It contains heterodyne receivers operating at frequencies between 118 and 664GHz which are sensitive to scattering by cloud ice particles, and has a flexible scanning geometry allowing both upward and downward views.

For downward-looking views from high altitude, representative of the satellite viewing geometry, the majority of the channels have a bias less than ± 1K. For most channels the biggest source of bias is thermal gradients in the heated calibration target. Standing waves due to coherent backscatter from the calibration targets are the dominant source of bias at 118 ± 3.0 and 664GHz. It is hoped that biases due to thermal gradients can be reduced in future by improved characterisation of the target temperatures. The NEΔT for downwards views in most channels is also less than 1K, and it is less than 2K for all channels other than 664-V. The presence of time-correlated noise in the receiver output prevents the NEΔT from being reduced by averaging a larger number calibration views.

Zenith brightness temperatures measured above the tropopause have been compared with radiative transfer simulations. The agreement is generally very good, and the differences are mostly consistent with the expected measurement uncertainties.

In future ISMAR will be used to validate radiative transfer models at submillimeter wavelengths for both clear and cloudy conditions, and to test retrieval algorithms for cloud ice properties. It can also be used for surface studies and post-launch calibration/validation for ICI. Additional receivers at 874.4GHz, which will give greater sensitivity to low ice water path and small ice particles, are currently being developed and will be integrated into ISMAR when they are available.

Atmospheric
Measurement
Techniques
Open Access
EGU
Discussions

References

Baran, A. J.: A new application of a multifrequency submillimeter radiometer in determining the microphysical and macrophysical properties of volcanic plumes: A sensitivity study, Journal of Geophysical Research, [Atmospheres], 117, doi:10.1029/2011JD016781, 2012.

Bizzari, B. et al.: GOMAS - Geostationary Observatory for Microwave Atmospheric Sounding, submitted to ESA in response to the call for
5   ideas for the Next Earth Explorer Core Missions, 2005.

Buehler, S., Jimenez, C., Evans, K., Eriksson, P., Rydberg, B., Heymsfield, A., Stubenrauch, C., Lohmann, U., Emde, C., John, V., et al.:
     A concept for a satellite mission to measure cloud ice water path, ice particle size, and cloud altitude, Quarterly Journal of the Royal
     Meteorological Society, 133, 109–128, doi:10.1002/qj.143, 2007.

Eriksson, P., Buehler, S., Davis, C., Emde, C., and Lemke, O.: ARTS, the atmospheric radiative transfer simulator, version 2, Jour-
10   nal of Quantitative Spectroscopy and Radiative Transfer, 112, 1551 – 1558, doi:http://dx.doi.org/10.1016/j.jqsrt.2011.03.001, http:
     //www.sciencedirect.com/science/article/pii/S0022407311001105, 2011.

Evans, K. and Stephens, G.: Microwave radiative transfer through clouds composed of realistically shaped ice crystals. Part II: remote sensing
     of ice clouds, Journal of the Atmospheric Sciences, 52, 2058–2072, doi:10.1175/1520-0469(1995)052<2058:MRTTCC>2.0.CO;2, 1995.

Evans, K. F., Walter, S. J., Heymsfield, A. J., and Deeter, M. N.: Modeling of submillimeter passive remote sensing of cirrus clouds, Journal
15   of Applied Meteorology, 37, 184–205, doi:10.1175/1520-0450(1998)037<0184:MOSPRS>2.0.CO;2, 1998.

Han, Y. and Westwater, E. R.: Analysis and improvement of tipping calibration for ground-based microwave radiometers, IEEE Transactions
     on Geoscience and Remote Sensing, 38, 1260–1276, doi:10.1109/36.843018, 2000.

Hersman, M. S. and Poe, G.: Sensitivity of the total power radiometer with periodic absolute calibration, IEEE Transactions on Microwave
     Theory and Techniques, 29, 32–40, doi:10.1109/TMTT.1981.1130283, 1981.

20   Hewison, T.: The design of Deimos: a microwave radiometer with channels at 23.8 GHz and 50.3 GHz for the UK Met. Research Flight C-
     130 aircraft, in: International Geoscience and Remote Sensing Symposium 'Quantitative Remote Sensing for Science and Applications',
     Firenze, Italy, vol. 3, pp. 2261–2263, doi:10.1109/IGARSS.1995.524165, 1995.

Jiménez, C., Buehler, S., Rydberg, B., Eriksson, P., and Evans, K.: Performance simulations for a submillimetre-wave satellite instrument to
     measure cloud ice, Quarterly Journal of the Royal Meteorological Society, 133, 129–149, doi:10.1002/qj.134, 2007.

25   Jones, D.: Validation of scattering microwave radiative transfer models using an aircraft radiometer and ground-based radar, Ph.D. thesis,
     University of Reading, 1995.

Kangas, V., D'Addio, S., Betto, M., Barre, H., Loiselet, M., and Mason, G.: Metop Second Generation microwave sounding and microwave
     imaging missions, in: Proceedings of the 2012 EUMETSAT Meteorological Satellite Conference, Sopot, Poland, Sept. 3-7, 2012.

McGrath, A. and Hewison, T.: Measuring the accuracy of MARSS-an airborne microwave radiometer, Journal of Atmospheric and Oceanic
30   Technology, 18, 2003–2012, doi:10.1175/1520-0426(2001)018<2003:MTAOMA>2.0.CO;2, 2001.

Murk, A., Duric, A., and Patt, F.: Characterization of ALMA calibration targets, in: Proc. 19th International Symposium on Space Terahertz
     Technology, 2008.

Rosenkranz, P. W.: Absorption of microwaves by atmospheric gases, in: Atmospheric remote sensing by microwave radiometry, edited by
     Janssen, M. A., pp. 37–90, John Wiley & Sons, Inc., ftp://mesa.mit.edu/phil/lbl_rt, 1993.

35   Rosenkranz, P. W.: Water vapor microwave continuum absorption: A comparison of measurements and models, Radio Science, 33, 919–928,
     doi:10.1029/98RS01182, 1998.

Atmospheric
Measurement
Techniques
Discussions

Rothman, L., Gordon, I., Babikov, Y., Barbe, A., Benner, D. C., Bernath, P., Birk, M., Bizzocchi, L., Boudon, V., Brown, L., Campargue, A., Chance, K., Cohen, E., Coudert, L., Devi, V., Drouin, B., Fayt, A., Flaud, J.-M., Gamache, R., Harrison, J., Hartmann, J.-M., Hill, C., Hodges, J., Jacquemart, D., Jolly, A., Lamouroux, J., Roy, R. L., Li, G., Long, D., Lyulin, O., Mackie, C., Massie, S., Mikhailenko, S., Müller, H., Naumenko, O., Nikitin, A., Orphal, J., Perevalov, V., Perrin, A., Polovtseva, E., Richard, C., Smith, M., Starikova, E., Sung, K., Tashkun, S., Tennyson, J., Toon, G., Tyuterev, V., and Wagner, G.: The HITRAN2012 molecular spectroscopic database, Journal of Quantitative Spectroscopy and Radiative Transfer, 130, 4 – 50, doi:10.1016/j.jqsrt.2013.07.002, http://www.sciencedirect.com/science/article/pii/S0022407313002859, HITRAN2012 special issue, 2013.

Staelin, D., Gasiewski, A., Kerekes, J., Shields, M., and Solman III, F.: Concept proposal for a Geostationary Microwave (GEM) Observatory, prepared for the NASA/NOAA Advanced Geostationary Sensor (AGS) Program, MIT, Lexington, Mass., p. 23, 1998.

Waliser, D. E., Li, J.-L. F., Woods, C. P., Austin, R. T., Bacmeister, J., Chern, J., Del Genio, A., Jiang, J. H., Kuang, Z., Meng, H., et al.: Cloud ice: A climate model challenge with signs and expectations of progress, Journal of Geophysical Research, 114, D00A21, doi:10.1029/2008JD010015, 2009.

Atmospheric
Measurement
Techniques

Open Access

EGU

Discussions

Table 1. ISMAR channel definitions (including planned upgrades)

Centre frequency (GHz)	Frequency offset (GHz)	IF Bandwidth (GHz)	Polarisation (at +50° downwards view)	Feature	System noise temperature (K)
118.75	±1.1	0.4	V	O_2	<700
	±1.5	0.4			<700
	±2.1	0.8			<700
	±3.0	1.0			<700
	±5.0	2.0			690
243.2	±2.5	3.0	V & H	Window	1850 (V) and 1700 (H)
325.15	±1.5	1.6	V	H_2O	2138
	±3.5	2.4			2085
	±9.5	3.0			2042
424.7	±1.0	0.4	V	O_2	optional upgrade
	±1.5	0.6			
	±4.0	1.0			
448.0	±1.4	1.2	V	H_2O	2500
	±3.0	2.0			3000
	±7.2	3.0			3500
664.0	±4.2	5.0	V & H	Window	2500 (V) and 2000 (H)
874.4	±6.0	3.0	V & H	Window	under development

Atmospheric
Measurement
Techniques
Discussions

Open Access

EGU

Table 2. Maximum typical calibration target temperature bias estimates and associated scene temperature biases during high-altitude flight

Receiver	δT_{hot}(K) Gradients	δT_{cold}(K) Gradients	δT_{hot}(K) Absorber	δT_{hot}(K) Standing wave	δT_{cold}(K) Standing wave	$\delta T_{\mathrm{scene,rje}}$(K) $K = 0.25$	$\delta T_{\mathrm{scene,rje}}$(K) $K = -2$
118 (other than ± 3.0)	+0.4	± 0.2	+0.3	0.0	0.0	-0.2 - 0.3	-2.0 - 0.6
118$\pm$3.0	+0.4	± 0.2	+0.3	-1.0	-1.0	-1.2 - 0.3	-5.0 - 2.6
243-H	+0.7	± 0.2	+0.3	0.0	0.0	-0.2 - 0.4	-2.6 - 0.6
243-V	+0.5	± 0.2	+0.3	0.0	0.0	-0.2 - 0.4	-2.2 - 0.6
325	+0.6	± 0.2	+0.3	0.0	0.0	-0.2 - 0.4	-2.4 - 0.6
448	+0.7	± 0.2	+0.3	0.0	0.0	-0.2 - 0.4	-2.6 - 0.6
664-H	+0.2	-0.2 - 0.1	+0.3	-1.5	-1.5	-1.7 - 0.2	-6.1 - 3.3
664-V	+0.3	-0.2 - 0.1	+0.3	-2.0	-2.0	-2.2 - 0.2	-7.8 - 4.3

Table 3. NEΔT estimates for ISMAR channels

Channel	Calculated NEΔT (K) $K = 0.5$	Calculated NEΔT (K) $K = -3.6$	Measured NEΔT (K) LN2 target ($K \approx -3.6$)
118$\pm$1.1	0.2	0.3	0.4
118$\pm$1.5	0.2	0.3	0.4
118$\pm$2.1	0.2	0.3	0.3
118$\pm$3.0	0.2	0.4	0.3
118$\pm$5.0	0.2	0.3	0.3
243-H	0.3	0.5	0.4
243-V	0.5	0.6	0.3
325$\pm$1.5	1.1	1.8	1.6
325$\pm$3.5	0.3	0.5	0.7
325$\pm$9.5	0.8	1.2	1.1
448$\pm$1.4	0.9	1.5	1.1
448$\pm$3.0	1.3	2.0	1.6
448$\pm$7.2	1.9	2.9	2.8
664-H	0.9	1.4	1.3
664-V	2.7	3.9	3.3

Atmospheric
Measurement
Techniques
Discussions

Figure 1. The location of the radiometer blister on the FAAM BAe-146 aircraft, and the ISMAR instrument installed in the blister with the cover removed
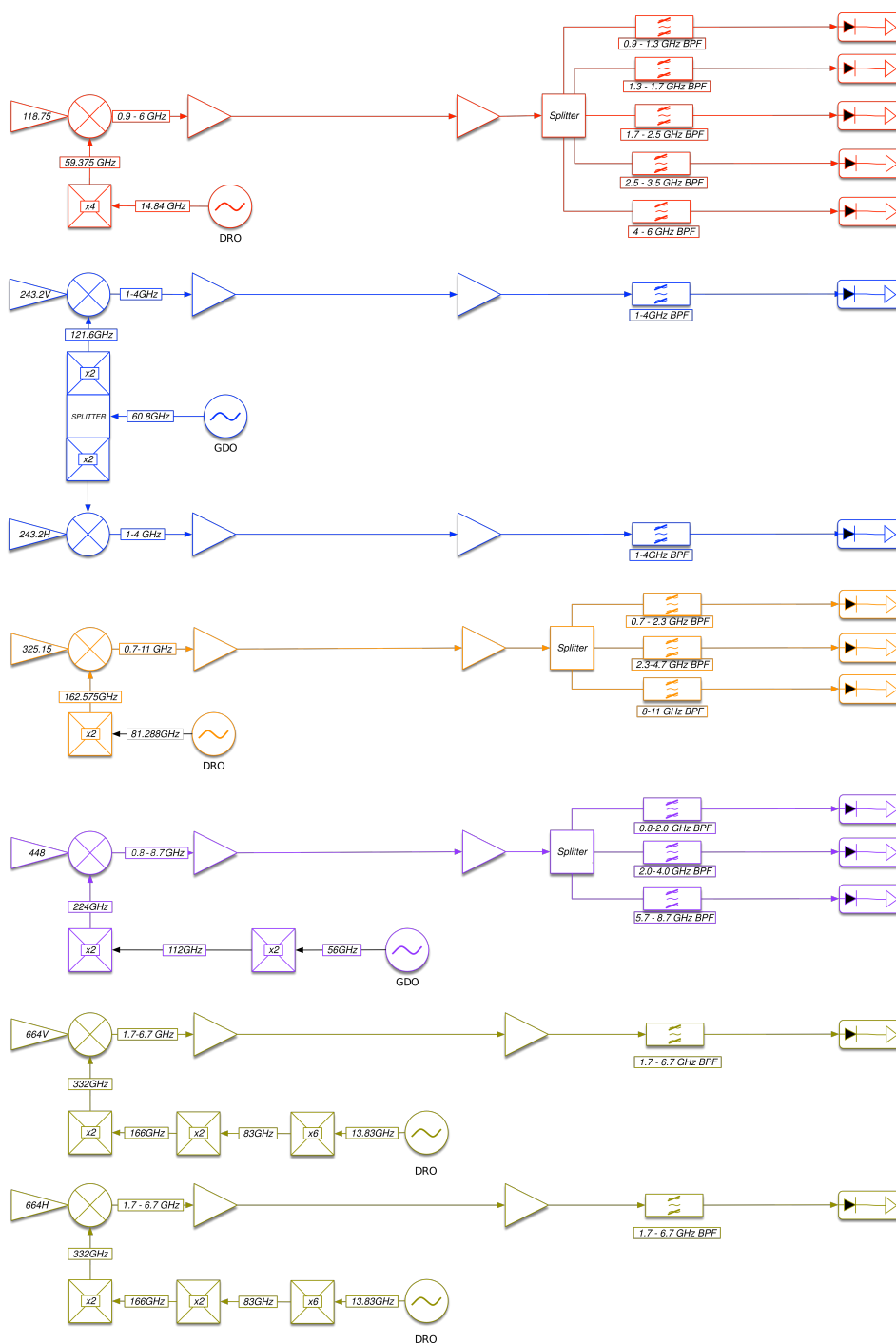
Atmospheric
Measurement
Techniques

Open Access
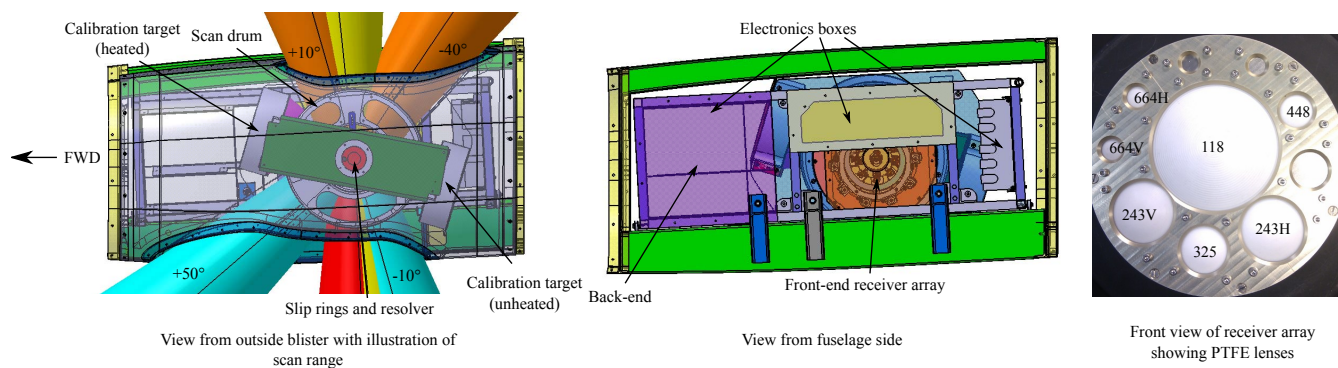
Discussions

EGU

Figure 2. Schematic of the ISMAR RF design

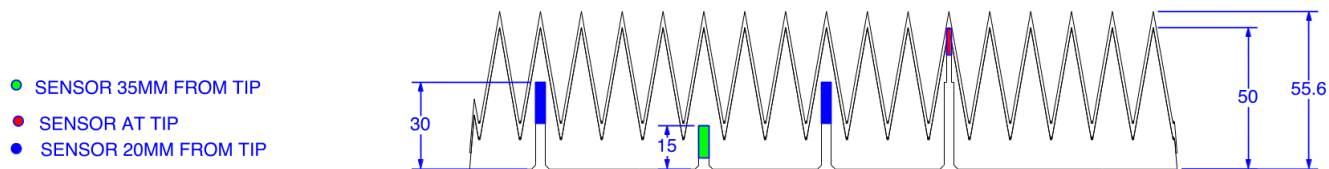**Figure 3.** Schematic of ISMAR with illustration of scan range, and image showing the front-end receiver array.

Figure 4. Cross-section of internal calibration target showing locations of PRTs
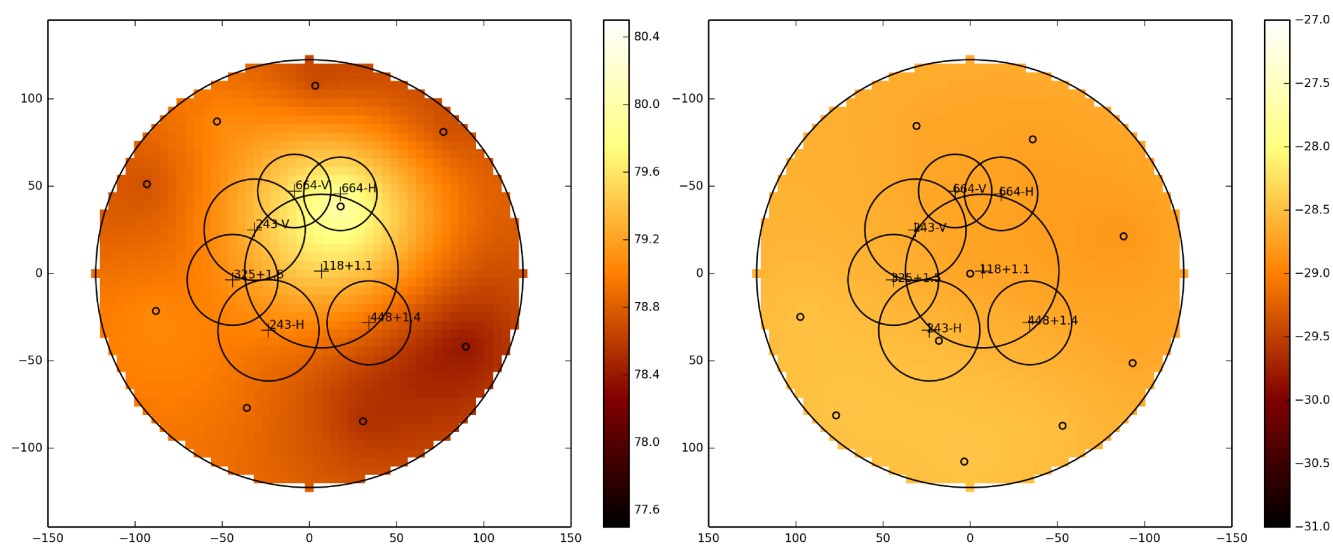
Figure 5. Hot (left) and ambient (right) calibration target temperature distribution during high-altitude flight. The small circles represent the locations of the PRTs and the colour shows the temperature (in Celsius) obtained by interpolating between the measurements. The -3dB footprint of the receivers is also indicated by the larger circles.
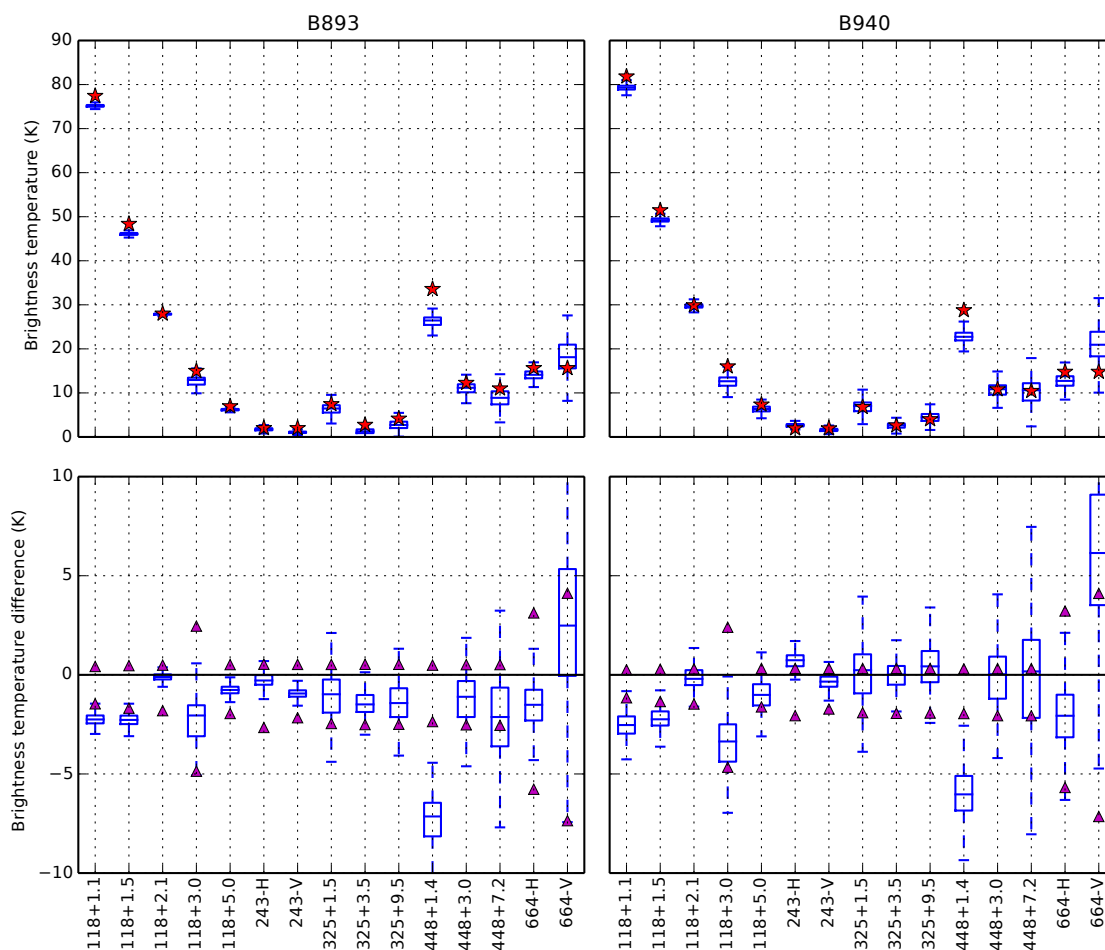
Atmospheric
Measurement
Techniques
Discussions

Open Access

EGU

Figure 6. Top: Zenith brightness temperatures during straight and level flight above the tropopause. The box-and-whiskers are the ISMAR measurements and the stars are simulations. Bottom: Difference between measurements and simulations. The triangles represent the estimated maximum bias in the measurements